IOP PUBLISHING PHYSICS IN MEDICINE AND BIOLOGY

Phys. Med. Biol. **53** (2008) 5343–5355 doi:10.1088/0031-9155/53/19/005

Photon and electron absorbed fractions calculated from a new tomographic rat model

P H R Peixoto[1,2], J W Vieira[3,4], H Yoriyaz[5] and F R A Lima[6]

[1] Departamento de Energia Nuclear, Universidade Federal de Pernambuco, Av. Prof. Luiz Freire 1000, Cidade Universitária, CEP 50740-540, Recife, PE, Brazil
[2] Centro Federal de Educação Tecnológica de Petrolina, Petrolina, PE, Brazil
[3] Centro Federal de Educação Tecnológica de Pernambuco, Recife, PE, Brazil
[4] Escola Politécnica, UPE, Recife, PE, Brazil
[5] Instituto de Pesquisas Energéticas e Nucleares, São Paulo, SP, Brazil
[6] Centro Regional de Ciências Nucleares-CNEN, Recife, PE, Brazil

E-mail: phrpeixoto@yahoo.com.br

Received 30 May 2008, in final form 29 July 2008
Published 29 August 2008
Online at stacks.iop.org/PMB/53/5343

Abstract

This paper describes the development of a tomographic model of a rat developed using CT images of an adult male Wistar rat for radiation transport studies. It also presents calculations of absorbed fractions (AFs) under internal photon and electron sources using this rat model and the Monte Carlo code MCNP. All data related to the developed phantom were made available for the scientific community as well as the MCNP inputs prepared for AF calculations in that phantom and also all estimated AF values, which could be used to obtain absorbed dose estimates—following the MIRD methodology—in rats similar in size to the presently developed model. Comparison between the rat model developed in this study and that published by Stabin *et al* (2006 *J. Nucl. Med.* **47** 655) for a 248 g Sprague–Dawley rat, as well as between the estimated AF values for both models, has been presented.

(Some figures in this article are in colour only in the electronic version)

1. Introduction

In nuclear medicine, internal sources of ionizing radiation are used for therapeutic or diagnosis purposes. Much of the progress in this field has been made by the use of experimental models, such as rats and mice, in preclinical tests. For appropriate absorbed dose–effect relationships to be obtained in the evaluation of new radiopharmaceuticals in these animals for radionuclide therapy, the absorbed dose in several organs and tissues must be determined as precisely as possible. As for humans, this can be accomplished with the development of an anatomic model (or phantom) for the considered organism, later inserting the data into a computer code

or an input file for Monte Carlo (MC) calculations. In addition, the necessary data include the mass density and the elemental composition of each modelled organ or tissue, the radiation sources specification and the MC tallies to be performed.

The most common methodology of calculating the absorbed dose $D(r_k)$ to a target region r_k from radiation emitted from a source region r_h is given by the MIRD formulation, defined by the MIRD Committee (Loevinger *et al* 1991). Its master equation is

$$D(r_k) = \tilde{A}(r_h)S(r_k \leftarrow r_h),$$

where $\tilde{A}(r_h)$ is the cumulated activity (or the total number of disintegrations in the relevant time interval) in the source region and $S(r_k \leftarrow r_h)$ is the average absorbed dose to the target region per radioactive disintegration in the source region. The cumulated activity is given by $\tilde{A}(r_h) = A_0(r_h)\tau_e$, where $A_0(r_h)$ is the initial activity in the source region and τ_e is the effective average life for the radionuclide in this region. Considering exponential biological excretion, we have $\tau_e = T_e/\ln 2$, with $T_e = T_p T_b/(T_p + T_b)$, where T_p, T_b, and T_e are, respectively, the physical, biological and effective half-lives of the nuclide in the source region. The S factor is given by $S(r_k \leftarrow r_h) = (1/m(r_k))\Sigma_i n_i(r_h)E_i(r_h)\phi_i(r_k \leftarrow r_h)$, where $m(r_k)$ is the mass for the target region, $n_i(r_h)$ is the average number of the i-type particles emitted (in the source region) per radioactive disintegration, $E_i(r_h)$ is the energy of such a particle and $\phi_i(r_k \leftarrow r_h)$ is the fraction of this energy that is absorbed by the target region. The $m(r_k)$ value depends on the computational model used for the organism under consideration, while $n_i(r_h)$ and $E_i(r_h)$ are taken from the emission spectrum of the nuclide in the source region. The absorbed fraction $\phi_i(r_k \leftarrow r_h)$ is estimated by Monte Carlo simulation, which involves the anatomy of the phantom.

Very few rat phantoms have been published to date. Konijnenberg *et al* (2004) developed a stylized model of a mature male Wistar rat. Three mature well-fed Wistar rats (average mass: 386 ± 35 g) were dissected and the dimensions and weights of several organs were measured. The relative positions of the segmented organs within the rat body were based on the photograph of a dissected rat as well as on the topologic capability of fitting all organs within the rat outer body contour. Most of the organs were modelled as ellipsoids. S factors for ^{90}Y, ^{111}In and ^{177}Lu, calculated using the Monte Carlo N-particle transport code system (MCNP), version 4C (Briesmeister 2000), were displayed, but absorbed fraction values were not tabulated. In the work of Stabin *et al* (2006), which also presents results for a mouse, a voxel-based rat model was built starting from CT images of a 248 g Sprague–Dawley rat. Calculations of absorbed fractions and S factors for ^{90}Y, ^{111}In, ^{131}I and ^{188}Re were performed using MCNP-4C, and the results were tabulated. Recently, a 3D whole body mouse atlas from CT and cryosection data was published (Dogdas *et al* 2007).

In this work, a tomographic phantom was developed from CT images of an adult male Wistar rat, and absorbed fractions were estimated using the MCNP-4C code for homogeneously distributed photon and electron internal sources. The results were presented in tables, so that one can obtain S factors from simple calculations, following the MIRD methodology. Comparisons with published data are also presented.

2. Materials and methods

2.1. Building the rat phantom

The construction of the rat phantom was accomplished in three different stages: (1) CT images acquisition, (2) segmentation and classification of the acquired images and (3) elemental composition and mass density specification for the rat phantom organs and tissues.

Table 1. Segmented organs and tissues, and identification numbers (IDs) reserved to them.

ID	Organ, tissue or region	Start slice	End slice
10	Air-outside	1	157
15	Body contour	2	156
20	Heart	50	62
25	Lungs	50	67
30	Liver	62	79
35	Stomach	68	83
40	Kidneys	74	91
45	Intestines	75	114
50	Spleen	77	88
55	Bladder	105	110
60	Testes	121	133
65	Skeleton	7	156
70	Other tissues	3	156

2.1.1. Primary CT image data. 155 axial tomographic images were collected for a 310 g and 100 days old adult male Wistar rat, using a PICKER SeleCT/SP CT scanner. The animal was kept in supine position and under anaesthesia (0.3 ml of thiopental) during imaging. The voxel dimensions were $0.71 \times 0.71 \times 1.5$ mm^3. A portion of the animal tail was not scanned; however, this fact is not relevant for internal dose estimates purposes.

2.1.2. Image segmentation and classification. In order to do the segmentation, one should have knowledge about rat anatomy and be able to identify organs to be segmented in each slice. A book of rat anatomy (Hayakawa *et al* 1997) was used as a reference. Also, a book of mouse anatomy (Iwaki *et al* 2001) was used as an auxiliary atlas specifically for the skeleton segmentation, because skeleton gross images are absent in the used rat atlas, and the rat and mouse skeleton are very similar. No semiautomatic segmentation technique was adopted. In contrast, an entirely manual segmentation was preferred, and, thus, image segmentation and classification happened simultaneously.

The body contour, skeleton, heart, lungs, testes, kidneys, spleen, stomach, liver and intestines were identified and segmented, in this order. In summary, for each segmented region, and it was segmented one region at a time (see table 1 for a list of regions), the following steps were accomplished. *Step 1*: the medical imaging software OSIRIS (Ligier *et al* 1994) was used for change in the window width (WW) and window level (WL) of the CT images, facilitating organ identification, and also for conversion from the original DICOM format to the 24 bits bitmap (BMP) format. *Step 2*: the obtained BMP images were segmented with the software PAINT (which is included in the Microsoft Windows accessories), with the aid of the adopted rat and mouse atlases. Organ form, dimensions and relative position were carefully analysed. *Step 3*: concluded the segmentation, the files were converted from the 24 bits BMP to the 8 bits BMP format and, then, through the software SCION IMAGE FOR WINDOWS (2002), for the text format. *Step 4*: from the generated text files a 3D matrix data file was created using the software FANTOMAS (Vieira 2004). *Step 5*: this matrix was then used as an entry for the software IDL (Research Systems Inc.), which generated 3D images of the segmented region. *Step 6*: some of these images were compared with organ photos from the used rat atlas, and with skeleton photos from the used mouse atlas, revealing satisfactory results.

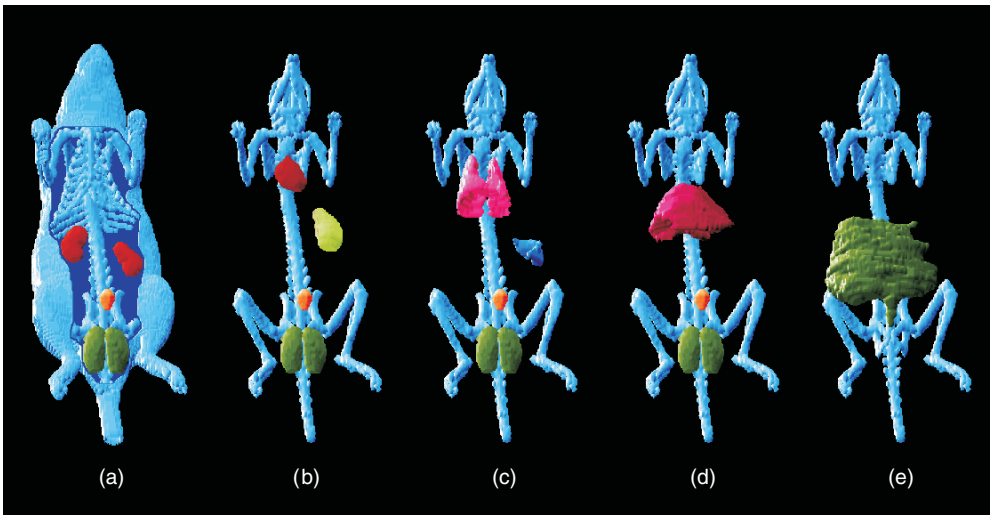

Figure 1. 3D images of the rat phantom showing (a) kidneys, bladder and testes; (b) heart and stomach; (c) lungs and spleen; (d) liver; (e) intestines.

Bladder was not identified in the CT images, but it was modelled in the rat phantom for comparisons with literature data. Its dimensions and positioning were estimated using the adopted rat atlas. All other not segmented phantom regions were classified as 'other tissues'. Figure 1 shows 3D images (generated by the software IDL) of all phantom organs, with no overlap among them.

All rat phantom organs have homogeneous composition and homogeneous density. No differentiation was made between wall and content in the segmentation of stomach and intestines. A same identification number (ID) was used for the two lungs. A similar procedure was adopted for kidneys, testes, and for small bowel and large bowel. Differentiation between small and large bowel was not attempted, mainly due to the intricate form as they are accommodated in the abdominal cavity. Inevitably, other tissues (like connective and adipose tissue) were included in the intestines segmentation. It was not possible to distinguish, in the CT images, the different types of tissues that constitute the skeleton, although in some images the central part of some bones have been found darker than in the periphery. It was the case, for instance, for the femur, which (in rats) has active (red) bone marrow in its core. Thus, a same ID was used for the skeleton as a whole. Of course, different IDs could be used for different skeleton parts, such as skull, vertebrae, pelvis, members, clavicles, shoulder blades, breastbone and ribs. However, it can be accomplished if there is interest, for instance, in obtaining absorbed fraction estimates to specific skeleton regions. Because the voxel dimensions of the developed phantom are one order higher than typical rat skin thickness, the body contour voxels are not representative of the rat skin. However, it is not a relevant fact, because doses received by the major abdominal organs in rats are usually of higher importance for internal dose assessment.

2.1.3. Elemental composition and mass density for the rat phantom organs and tissues. The elemental composition and mass density for the phantom organs and tissues were taken from the International Commission on Radiation Units and Measurements (ICRU) Report 46 (ICRU 1992), except in the case of skeleton, for which the bone and marrow mixture used by Cristy

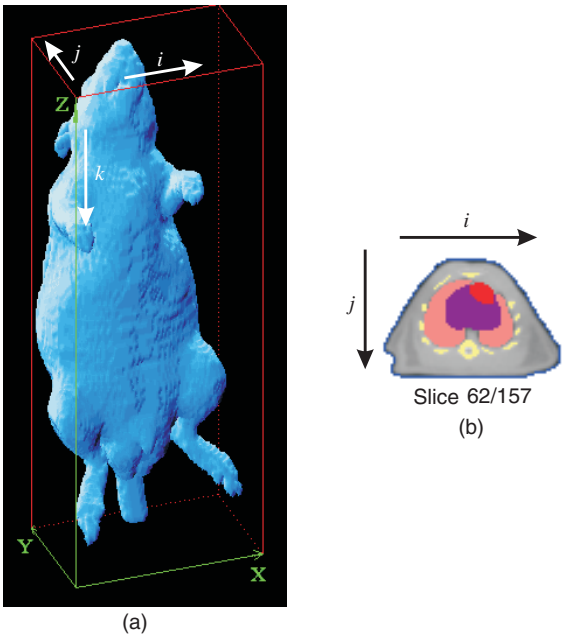

Figure 2. Variation direction of matrix element indices i, j and k: (a) 3D view of the rat phantom and coordinate system used; (b) caudal view of slice 62/157 showing heart (red), liver (purple), lungs (pink) and some skeletal features (yellow).

and Eckerman (1987) was adopted. The calculated total mass of the rat phantom is 276.80 g, and, thus, it is about 11% lower than the mass of the used specimen (310 g)—an acceptable difference, considering the approximations in the model. Because the tissue compositions and densities used were for human tissue rather than rat tissue, it is expected that this introduced an additional error in the calculated absorbed fractions.

2.2. Implementing the rat phantom into MCNP and preparing the input files for absorbed dose calculations

After the construction of the rat phantom, the next step in the development of the model for Monte Carlo organ dose calculations was to prepare the MCNP input files containing all information related to the phantom.

2.2.1. Necessary information for implementing the rat phantom into a computer code (or an input file) for dose assessment. Independently of the chosen software for dose assessment, all the information presented below is necessary to perform calculations with the developed rat phantom.

The spatial distribution of voxels is given by a 118 × 76 × 157 3D matrix, whose elements are the IDs of the different regions that constitute the phantom. The matrix element a_{ijk} corresponds to the voxel at column i ($1 \leqslant i \leqslant 118$; from left to right) and line j ($1 \leqslant j \leqslant 76$; from front to back) of slice k ($1 \leqslant k \leqslant 157$; from top to bottom), see figure 2. The amount of slices is 157 (and not 155—the amount of collected tomographic images) because two hollow slices were added to the phantom: one above the slice corresponding to the start tomographic image and one below the slice corresponding to the end tomographic image. This matrix is

saved in a file named RAT3D.dat (it should be requested by e-mail from the corresponding author). There are two versions: text format and binary format. Reading the matrix elements in the RAT3D.dat file, the first index to vary is the i index, the second is the j index and the third is the k index. Therefore, the first read element in the RAT3D.dat file is a_{111}, the second read element is a_{211}, the third read element is $a_{311}, \ldots$, the 119th read element is $a_{121}, \ldots$, the penultimate element is $a_{117\,76\,157}$ and the last element is $a_{118\,76\,157}$.

Table 1 associates, with each ID in the RAT3D.dat file, an organ, tissue or region. Note the presence of air voxels in the table. Those voxels are all external to the phantom.

The pixel dimensions are 0.71 mm × 0.71 mm, and the slice thickness is 1.5 mm, so that the voxel dimensions are 0.71 mm × 0.71 mm × 1.5 mm.

The elemental composition and the mass density used in the Monte Carlo calculations were taken from ICRU-46 (except for skeleton, as already pointed). The data taken from ICRU-46 are named there as *skin–adult* (used for body contour), *heart–adult–blood-filled*, *lung–adult–healthy–inflated*, *liver–adult–healthy*, *GI tract–adult* (used for stomach and intestines), *kidney–adult*, *spleen–adult*, *urinary bladder–adult–filled*, *testis–adult*, *average soft tissue–adult–male* (used for 'other tissues').

2.2.2. MCNP inputs. MCNP input files for absorbed fraction calculations were created starting from the above-presented data for the developed rat phantom. To these files data on radiation sources were added, and also Monte Carlo tally type and some other data. Eleven uniform source regions were considered—body contour, heart, lungs, liver, stomach, kidneys, intestines, spleen, bladder, testes, and skeleton—and were adopted the discrete initial energies 0.01, 0.015, 0.02, 0.03, 0.05, 0.1, 0.2, 0.5, 1, 2 and 4 MeV for photons, and 0.1, 0.2, 0.4, 0.7, 1, 2 and 4 MeV for electrons, resulting in 198 MCNP input files. The difference among those input files (which could be requested by e-mail from the corresponding author) is only in the specification of radiation source, which changes when the source region, the source particle type (photon or electron) or the particle energy is modified. In all simulations performed in this work the PE transport mode (transport of secondary particles included) was adopted, and the number of histories was fixed to 2400 000—sufficient to reduce the estimated relative errors (R) for all calculated self-absorbed fractions to very low values ($0.0003 \leqslant R \leqslant 0.0096$ for photons and $0.0001 \leqslant R \leqslant 0.0008$ for electrons) and to low values for most cross-absorbed fractions (for instance, for liver as a source and heart as a target it was found $0.0065 \leqslant R \leqslant 0.0159$ for photons and $0.0038 \leqslant R \leqslant 0.0467$ for electrons). No variance reduction technique was used. Electron and photon histories were run on a multimode-computed cluster running *Woody Debian Linux*, and made of 11 AMD Athlon XP 1800+ 1.53 GHz CPU with 512 MB RAM plus one server with the same CPU and 1 GB RAM. It roughly took 1 month to run the whole task.

An outside air sphere (with 24 cm radius) involving the rat phantom was included in the MCNP input files, which allowed us to simulate the backscatter radiation. The mass density and the elemental composition (weight fractions) adopted for the air in the sphere (and in the air-outside voxels) were, respectively, 0.001 205 g cm^{-3}, and 75.5% N, 23.2% O and 1.3% Ar.

3. Results and discussions

3.1. Comparison between the developed rat phantom and other models

Anatomic variations among rats of the same or of different species can be considerable, and this places a limit on the accuracy of dosimetry in these small animals. Thus, anatomic

Table 2. Masses for the rat organs for this study and values reported in other investigations.

	Organ or tissue mass (g)		
Organ or tissue	This study	Stabin *et al* (2006)	Konijnenberg *et al* (2004)
Body contour	22.69	–	–
Heart	1.66	1.48	1.8
Lungs	0.94	1.92	3.2
Liver	11.68	9.64	21.9
Stomach	2.75	2.53	6.2
Kidneys	2.10	2.22	3.4
Intestines	22.72	34.24	24.5
Spleen	0.58	0.42	0.8
Bladder	0.16	0.92	0.27
Testes	2.67	–	3.6
Skeleton	23.06	–	–
Other tissues	185.79	–	–

comparisons among rat phantoms are particularly important in interpreting radiation dose estimates to those models.

Table 2 shows the organ mass values for the rat phantom developed in this study and the values reported by Konijnenberg *et al* and Stabin *et al* for their rat phantoms. Except for lungs, bladder and intestines, the values reported here are relatively in line with the values published by Stabin *et al*. The mass values for the heart, liver, stomach and spleen in our rat phantom are slightly higher than the mass values for the corresponding organs in the Stabin *et al* rat phantom, while the mass for kidneys is slightly smaller. Comparison between the intestines masses for these two models is difficult, because in both models other tissues were included in the organ segmentation; nevertheless, the values are of the same order. However, note that the value found by Stabin *et al* is even larger than the value used by Konijnenberg *et al*, which is for a much heavier rat. The same occurs to bladder, which has comparatively higher mass value than in the Stabin *et al* rat phantom (and this is reflected in the comparatively higher estimated absorbed fractions to this organ). But the bladder masses presented in table 2 include wall and content, and the bladder content mass is a quantity that can vary substantially. The lungs of the rat phantom developed in this study have low mass, in comparison with values for the other two models. However, any adjustment in the size of the developed rat phantom lungs did not seem reasonable. Due to their low density, they are among the more easily identified organs in the CT images and, thus, their segmentation is the most reliable (as for skeleton). No testes were segmented in the Stabin *et al* rat phantom.

3.2. AFs for photons and electrons

All calculated absorbed fractions for the simulated internal sources, and the corresponding estimated relative errors (R), are presented on 11 supplemental tables for photons and on 11 supplemental tables for electrons available online stacks.iop.org/PMB/53/5343. For a given random variable X, R is defined as $\sigma_{\bar{x}}/\bar{x}$, where $\bar{x}$ is the Monte Carlo mean of X and $\sigma_{\bar{x}}$ is the estimated standard deviation of the mean (Briesmeister 2000).

Figure 3 shows self-absorbed fraction plots for photons in the source regions of the developed rat model. All curves in this figure present a steep descent from 0.01 MeV to 0.1 MeV (showing that, for this energy range, photon escape from the source regions rapidly increases as energy grows), with a local minimum at 0.1 MeV (except for skeleton, which

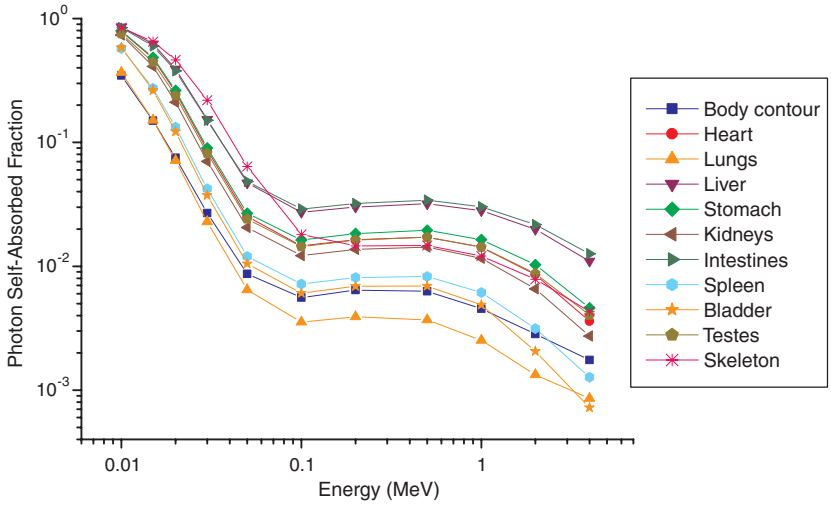

Figure 3. Self-absorbed fractions for photons in the source regions.

presents a local minimum at 0.2 MeV). After these relative minima, photon self-absorbed fractions have a slight increase and then turn to decrease. This behaviour, common to all curves in figure 3, essentially corresponds to the form as the energy-absorption coefficient varies with emitted photon energy in the source regions (see the review article by Turner (2004) for a discussion on energy-absorption coefficient as a function of energy for photons in water, which well approximates soft tissue). For the same energy, differences in the self-absorbed dose values are mainly due to variations in mass and/or shape of the source regions. Both factors must be considered jointly. For instance, although the intestines mass is almost two times the liver mass, the relatively thinner shape of intestines contributes to a larger escape of particles from them, and the result is that photon self-absorbed fractions for liver and intestines have very near values. On the other hand, although the body contour mass is essentially the same as the intestines mass, because of the fact that the shape of body contour is very thin it has as a consequence photon self-absorbed fractions lower than for intestines. Elemental composition and mass density variations have a lesser effect on the photon self-absorbed fractions, except for lungs and skeleton, which deviate substantially from average soft tissue. For lungs, in spite of their great volume, their low density implicates the smallest photon self-absorbed fractions for almost all energy values considered. Note that the plots for heart, stomach, kidneys and testes in figure 3 are relatively close, and this is a consequence of their closer mass values and their similar shapes. The kidneys have lower photon self-absorbed fractions than heart, although the former have a larger mass than heart, because this mass is distributed between two organs. Except for lungs and body contour (whose low photon self-absorbed fraction values already have the given particular explanation), the lowest photon self-absorbed fractions occur to bladder and spleen, which are the two phantom organs with the smallest masses.

Figure 4 shows photon absorbed fraction plots for liver as the source organ. The points whose corresponding R values have been 0 or 1 were removed from the graph. For the remaining points, the R values are larger than 0.10 only to bladder (for all considered energy) and to spleen (for 0.01 MeV only) and testis (for 0.02 MeV only). In the case of bladder, the R values are sufficiently low ($0.1118 \leqslant R \leqslant 0.2345$) for a pattern to be observed (absorbed

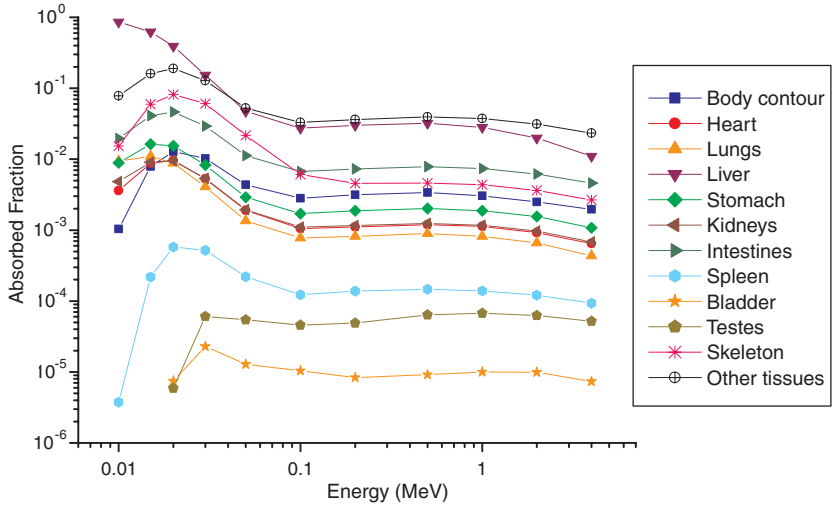

Figure 4. Photon absorbed fractions for liver as a source.

fraction plots with high R values are of low usefulness for internal dose assessment because reliable dose conversion factors for a given nuclide cannot be estimated).

The highest difference between the common shape of curves in figure 3 and the common shape of curves in figure 4 (except for liver, which is the source organ) occurs for the lower energy values. In that region of figure 4, an initial growth can be seen that is approximately the opposite (in qualitative terms) of what occurs in figure 3, for the same energy values. This behaviour is related to the increase in the number of particles that escape from the source organ, and, consequently, to the increase in the number of particles that deposit energy in the several adjacent target regions, as the initial energy of the photons increases. For each target region, after a given photon initial energy the number of particles that deposit energy out of the considered target or escape from the phantom increases, and this explains the first peaks in figure 4. Note that these peaks occur at lower energy values for the target regions closer the source organ, such as lungs and stomach, and at higher energies for the target regions far away from the source organ, such as bladder and testes (however, these peak locations can change slightly by increasing the number of points in the abscissa axis). For the same energy and the same source organ, differences among the absorbed fraction values occur due to shape and mass variations among the several target regions, and, mainly, due to variations in the relative distance between source and target regions.

It is very important to observe that organs that present higher absorbed fractions do not necessarily present higher absorbed dose values. Consider, for instance, lungs and intestines. Figure 4 shows that, for all energies in the graph, the absorbed fractions are lower for lungs than for intestines. However, for these same energies, the specific absorbed fractions are higher for lungs than for intestines. Thus, the absorbed doses, due to (0.01–4 MeV) photon emission in liver, are higher in lungs than in intestines. In this sense, the specific absorbed fractions are more informative than absorbed fractions. On the other hand, interpreting absorbed fraction versus energy graphics is easier than interpreting specific absorbed fraction versus energy graphics, because in the last case the organ mass values must always be considered.

Figure 5 shows self-absorbed fraction plots for electrons in the source regions of the developed rat model. All curves in this figure decrease monotonically with energy. Also, the

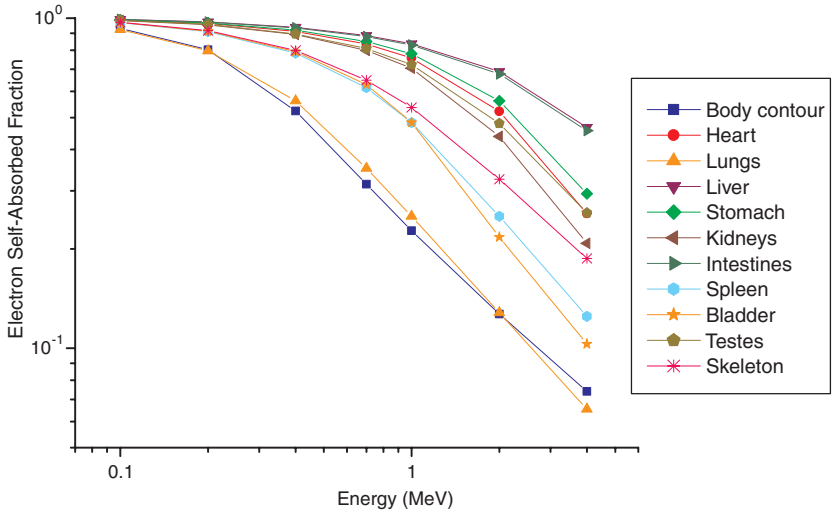

Figure 5. Self-absorbed fractions for electrons in the source regions.

initial decrease is moderate, showing that—in contrast to the photon self-absorbed fraction curves—the particle escape from the source regions initially grows slowly with energy. For 0.1 MeV or less, the initial electron energy is almost completely absorbed in the source regions. However, as the initial electron energy grows, the self-absorbed fractions decrease sufficiently for that they cannot reasonably be considered equal to 1. Several common characteristics can be noticed between plots in figure 3 and plots in figure 5. For instance, in both graphics, the self-absorbed fractions for lungs are among the lowest ones, and the curves for heart, stomach, kidneys and testes are relatively close.

Figure 6 shows electron absorbed fraction plots for liver as the source organ. The points whose corresponding R values have been higher than 0.10 were removed from the graph (except for body contour at 0.1 MeV, for which $R = 0.1722$). As expected, while in figure 5 all curves decrease monotonically with energy, in figure 6 all curves increase monotonically with energy, except for liver, which is the source organ, and also for lungs. In this last case, the fraction of particles that escape or deposit energy at more distant regions, out of the lungs, increases for energies above 2 MeV, and it induces a relative maximum at this energy value. The existence of such a relative maximum is expected for the other target regions at energies above 4 MeV (note that in figure 4 the first local maximum occurs early to lungs than to most other target regions). The adjacent regions to the source organ ('other tissues', intestines, skeleton, stomach, lungs, kidneys and heart) almost always present the higher absorbed fraction values. The body contour curve in figure 6 has a peculiar shape, changing its steepness around 0.7 MeV. The origin of this behaviour is that, for low energies, electrons have low range in matter; however, starting from around 0.7 MeV, it grows considerably the number of electrons that deposit energy in the body contour, and thus the absorbed fraction in the body contour then increases faster.

3.3. Absorbed fractions comparisons

In general, the absorbed fractions found in this study are consistent with those presented by Stabin *et al* for a Sprague–Dawley rat phantom, and, in some cases, the estimated values in

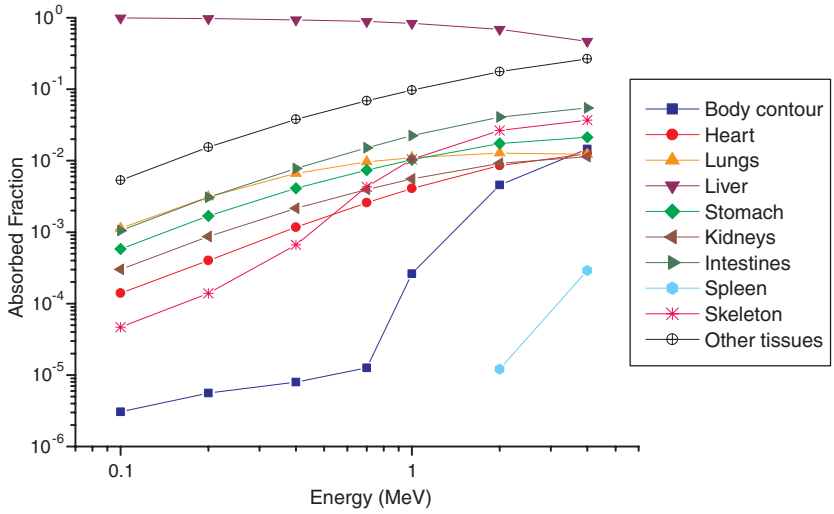

Figure 6. Electron absorbed fractions for liver as a source.

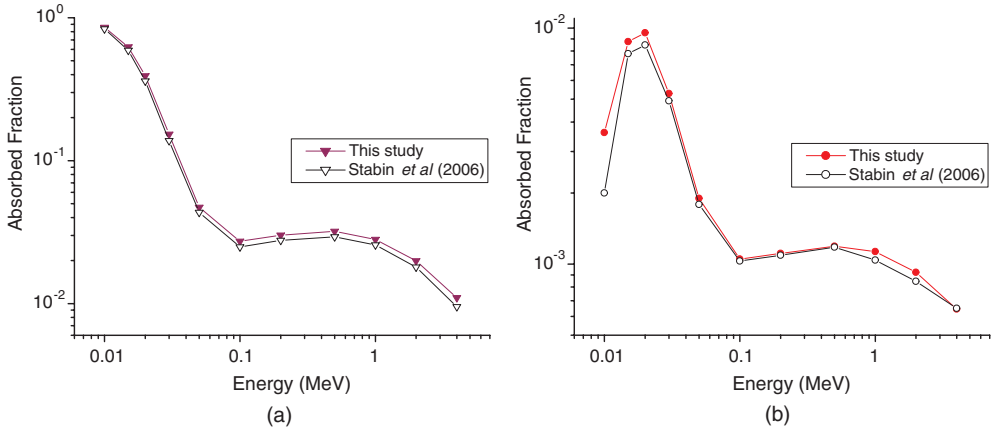

Figure 7. Photon absorbed fractions for liver as a source: (a) liver as a target and (b) heart as a target.

both works are very close. However, the comparisons indicate that anatomic variations in these small animals have a noticeable effect in the estimated absorbed fraction values, especially for electrons. It is not a surprising result, because Hindorf *et al* (2004) have already showed this aspect for mice. Figures 7 and 8 show, respectively, photon and electron absorbed fraction plots for liver as the source organ. Except in figure 8(b) (below 2 MeV), the results from this study are close to those found by Stabin *et al*. The divergence between the curves in figure 8(b), below 2 MeV, indicates that, for low energy electron sources, anatomic differences between the models are determinant to differences in dose calculations.

Differences in the number of simulated histories must also be a relevant factor to some of the observed divergences between the absorbed fractions calculated in this study and those presented by Stabin *et al*. A positive factor is that the calculation performed by Stabin *et al* has

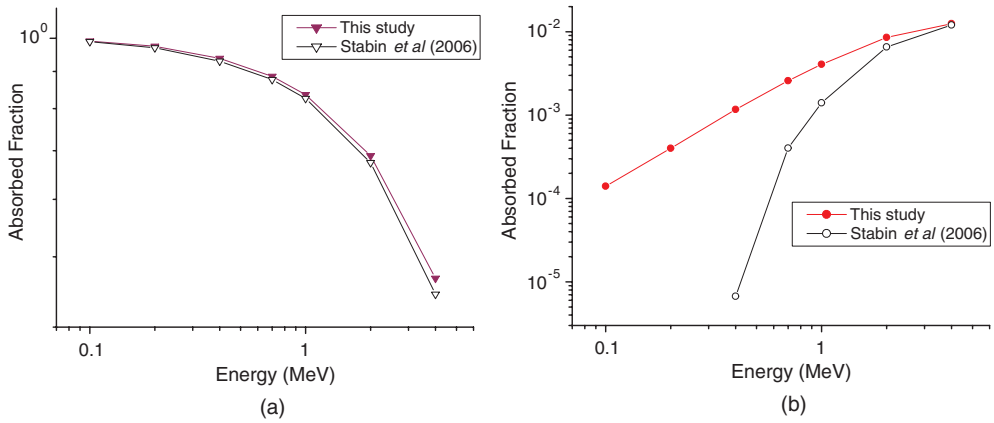

Figure 8. Electron absorbed fractions for liver as a source: (a) liver as a target and (b) heart as a target.

been made with the MCNP-4C computer code—the same code used in this study; therefore, there was no change in the AF results due to change in the transport computer code.

4. Conclusions

A voxel-based adult male Wistar rat phantom was developed starting from 155 axial CT images of a 310 g and 100 days old specimen in supine position. All data related to the phantom were made available for the scientific community.

The calculated absorbed fractions, presented in the 22 supplemental tables (available online) stacks.iop.org/PMB/53/5343, could be used—following the MIRD methodology—to obtain absorbed dose estimates in rats similar in size to the developed phantom. However, some information on the bio distribution or on the bio kinetics of the considered radiopharmaceutical will be necessary for correctly calculating the initial activities in the source organs and also the effective half-lives.

In most cases, the calculated organ masses in this study agree relatively well with those presented by Stabin *et al* (2006) for a 248 g voxel-based Sprague–Dawley rat phantom. However, comparisons made between the AF results for these two models indicate that anatomic variations in these small animals have a notable effect on the estimated absorbed fraction values, as have been already pointed out by Hindorf *et al* (2004) for mice.

Acknowledgments

We are grateful for the financial support of the Brazilian agency CNPq. PHRP acknowledges a CNPq fellowship.

References

Briesmeister J F 2000 MCNP: A General Monte Carlo *N*-Particle Transport Code, version 4C (NM: Los Alamos National Laboratory)

Cristy M and Eckerman K F 1987 Specific absorbed fractions of energy at various ages from internal photon sources *Report No ORNL/TM-8381 V1-V7* (Oak Ridge, TN: Oak Ridge National Laboratory)

Dogdas B, Stout D, Chatziioannou A F and Leahy R M 2007 Digimouse: a 3D whole body mouse atlas from CT and cryosection data *Phys. Med. Biol.* **52** 577–87

Hayakawa T, Yamashita H and Iwaki T 1997 *A Color Atlas of Sectional Anatomy of Rat* (Tokyo: Chikusan Publishing Co.)

Hindorf C, Ljungberg M and Strand S-E 2004 Evaluation of parameters influencing *S* values in mouse dosimetry *J. Nucl. Med.* **45** 1960–5

ICRU 1992 Photon, Electron, Proton and Neutron Interaction Data for Body Tissues *ICRU Report 46* (Bethesda, MD: ICRU)

Iwaki T, Yamashita H and Hayakawa T 2001 *A Color Atlas of Sectional Anatomy of the Mouse* (Tokyo: Adthree Publishing Co.)

Konijnenberg M W, Bijster M, Krenning E P and De Jong M 2004 A stylized computational model of the rat for organ dosimetry in support of preclinical evaluations of peptide receptor radionuclide therapy with 90Y, 111In, or 177Lu *J. Nucl. Med.* **45** 1260–9

Ligier Y, Ratib O, Logean M and Girard C 1994 Osiris: a medical image manipulation system *M. D. Comput.* **11** 212–8

Loevinger R, Budinger T F and Watson E E 1991 *MIRD Primer for Absorbed Dose Calculations* (New York, NY: The Society of Nuclear Medicine)

Scion Image for Windows 2002 Online at http://www.scioncorp.com (Frederick, MD: Scion Corporation) (accessed on November 2002)

Stabin M G, Peterson T E, Holburn G E and Emmons M A 2006 Voxel-based mouse and rat models for internal dose calculations *J. Nucl. Med.* **47** 655–9

Turner J E 2004 Interaction of ionizing radiation with matter *Health Phys.* **86** 228–52

Vieira J W 2004 *DSc Thesis* Universidade Federal de Pernambuco, Recife, PE, Brazil